Structural Insight into the Ion-Exchange Mechanism of the Sodium/Calcium Exchanger

Jun Liao *et al.*

Science **335**, 686 (2012);
DOI: 10.1126/science.1215759

Science (print ISSN 0036-8075; online ISSN 1095-9203) is published weekly, except the last week in December, by the American Association for the Advancement of Science, 1200 New York Avenue NW, Washington, DC 20005.

Structural Insight into the Ion-Exchange Mechanism of the Sodium/Calcium Exchanger

Jun Liao,[1]* Hua Li,[1,2]* Weizhong Zeng,[1,2] David B. Sauer,[1] Ricardo Belmares,[1]† Youxing Jiang[1,2]‡

Sodium/calcium (Na^+/Ca^{2+}) exchangers (NCX) are membrane transporters that play an essential role in maintaining the homeostasis of cytosolic Ca^{2+} for cell signaling. We demonstrated the Na^+/Ca^{2+}-exchange function of an NCX from *Methanococcus jannaschii* (NCX_Mj) and report its 1.9 angstrom crystal structure in an outward-facing conformation. Containing 10 transmembrane helices, the two halves of NCX_Mj share a similar structure with opposite orientation. Four ion-binding sites cluster at the center of the protein: one specific for Ca^{2+} and three that likely bind Na^+. Two passageways allow for Na^+ and Ca^{2+} access to the central ion-binding sites from the extracellular side. Based on the symmetry of NCX_Mj and its ability to catalyze bidirectional ion-exchange reactions, we propose a structure model for the inward-facing NCX_Mj.

Calcium signaling is essential for many physiological processes, including muscle contraction, cell mobility, fertilization, exocytosis, and apoptosis (*1*, *2*). One of the major players in regulating intracellular Ca^{2+} in eukaryotes is the Na^+/Ca^{2+} exchanger (NCX) (*3*–*5*), a Ca^{2+} transporter that can extrude intracellular Ca^{2+} across the cell membrane against its chemical gradient by using the downhill gradient of Na^+. For example, in cardiac myocytes, elevated cytosolic free Ca^{2+} required for muscle contraction must be removed rapidly to ensure relaxation. This clearance is carried out by the cardiac exchanger NCX1 (*6*), which extrudes Ca^{2+} into the extracellular space, and Ca^{2+} pumps, which restore Ca^{2+} into the sarcoplasmic reticulum. Several functional features of NCX define its physiological roles: It can exchange Ca^{2+} and Na^+ with a high turnover rate (*7*, *8*); the ion-exchange process is electrogenic, with a stoichiometry of three Na^+ for one Ca^{2+} (*8*–*13*); and the exchange reaction is bidirectional, depending on the membrane potential and the chemical gradient of Na^+ and Ca^{2+} (*3*). Because of its abundance in various tissues and its essential roles in Ca^{2+} homeostasis, dysfunctions of the Na^+/Ca^{2+} exchanger are associated with many human pathologies, including cardiac hypertrophy, arrhythmia, and postischemic brain damage (*3*, *14*, *15*).

Predicted to possess nine membrane-spanning helices, the transmembrane domain of the eukaryotic NCX is separated into two parts in primary sequence by a large intracellular regulatory domain (*4*, *5*, *16*, *17*). Interestingly, the removal of this intracellular domain still yields a highly active Na^+/Ca^{2+} exchanger, indicating that the transmembrane portion of the NCX constitutes the basic functional unit for ion transport (*18*, *19*). All NCX proteins contain two highly conserved homologous sequence motifs called α repeats, one on each part of the transmembrane domain, that are believed to arise from a gene-duplication event (*4*, *20*, *21*). Mutagenesis studies have demonstrated that both motifs are important for ion binding and translocation (*4*, *22*). The presence of the two homologous repeats is also the hallmark of other members of the cation-Ca^{2+} exchanger superfamily, most notably the NCKX family (*23*), a K^+-dependent Na^+/Ca^{2+} exchanger that was first found in the vertebrate eye (*24*), and microbial NCX homologs, which lack the large intracellular regulatory domain (*4*, *21*). To reveal the structural basis of the ion-exchange mechanism in NCX, we characterized the Na^+/Ca^{2+}-exchange function of an NCX homolog from *Methanococcus jannaschii*, named NCX_Mj, and determined its crystal structure to 1.9 Å resolution.

NCX_Mj functions as a Na^+/Ca^{2+} exchanger. We employed a $^{45}Ca^{2+}$ flux assay to determine the exchange function of NCX_Mj (*25*). Purified NCX_Mj was reconstituted into liposomes loaded with a buffer solution containing 120 mM NaCl, 30 mM KCl, and 1 μM $CaCl_2$ (buffered with EGTA) at pH 6.5. Ca^{2+} influx was initiated by exchanging the extraliposomal solution with a reaction buffer containing various concentrations of NaCl, KCl, and radioactive $^{45}CaCl_2$ and monitored by measuring the time-dependent accumulation of liposomal radioactivity (Fig. 1A). In the absence of any ionic gradient (the reaction buffer is the same as intraliposomal solution), we observed a slow influx of $^{45}Ca^{2+}$, probably due to the NCX_Mj-mediated Ca^{2+}/Ca^{2+} exchange (curve 1). Whereas an inward Ca^{2+} gradient promoted the influx of Ca^{2+} (curve 2, with 33 μM extraliposomal $^{45}CaCl_2$), the rate of Ca^{2+} influx was substantially enhanced by an outwardly directed Na^+ gradient (curve 3, with 60 mM extraliposomal NaCl), consistent with the behavior of

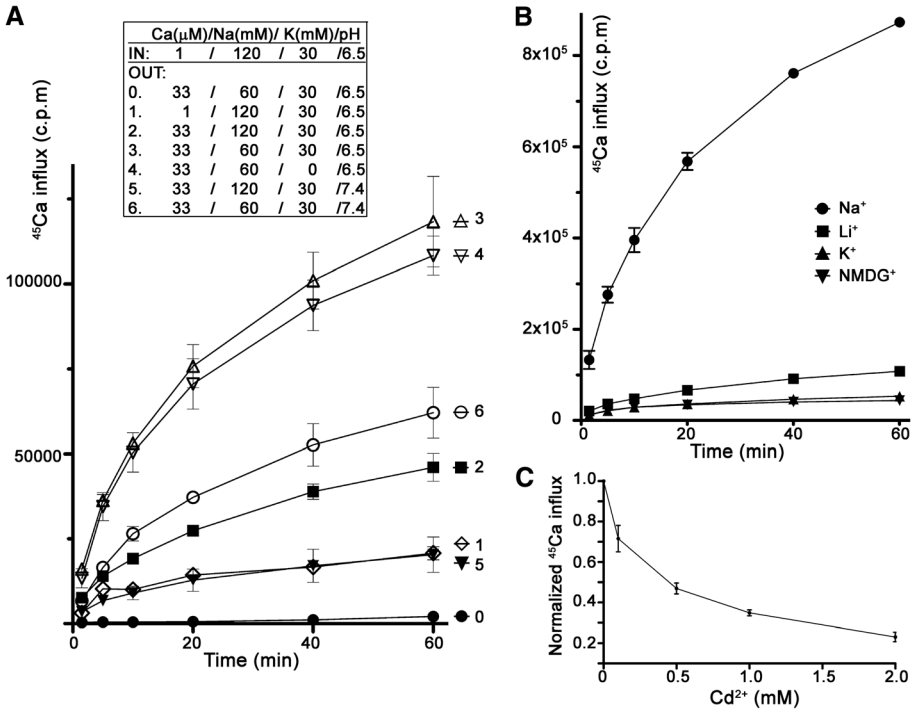

Fig. 1. $^{45}Ca^{2+}$ flux assays of NCX_Mj reconstituted liposomes. (**A**) Curves 1 to 6 show the time-dependent $^{45}Ca^{2+}$ influx with various extraliposomal reaction solutions, as listed in the inset. Curve 0 is the control assay using liposomes deficient of protein. The intraliposomal solution remains the same in all measurements. c.p.m., counts per minute. (**B**) Selectivity of NCX_Mj. The intraliposomal solution contained 120 mM of either Na^+, K^+, Li^+, or $NMDG^+$ as the only monovalent cation. The extraliposomal reaction solution contained 120 mM $NMDG^+$ and remained the same in all measurements. (**C**) Cd^{2+} blockage of NCX_Mj. The reaction solution is the same as that used for curve 3 in (A), except containing various concentrations of $CdCl_2$. The Ca^{2+} influx was terminated 20 min after adding $^{45}CaCl_2$. All data points are mean ± SEM of two independent experiments. Some data points shown in (B) contain error bars smaller than the representative symbols.

[1]Department of Physiology, University of Texas Southwestern Medical Center, Dallas, TX 75390–9040, USA. [2]Howard Hughes Medical Institute, University of Texas Southwestern Medical Center, Dallas, TX 75390–9040, USA.

*These authors contributed equally to this work.
†Present address: North Crowley High School, Fort Worth, TX 76123, USA.
‡To whom correspondence should be addressed. E-mail: youxing.jiang@utsouthwestern.edu

a Na^+/Ca^{2+} exchanger. This Na^+-facilitated Ca^{2+} influx is independent of K^+, as the removal of the extraliposomal KCl did not affect the rate of Ca^{2+} influx (curve 4). To test if NCX_Mj could be a H^+/Ca^{2+} exchanger, we performed a similar assay in an extraliposomal reaction solution of pH 7.4 (versus pH 6.5 inside). In the absence of a Na^+ gradient, the outward proton gradient actually reduces the influx of Ca^{2+} (curve 5), which can be partially alleviated by establishing an outwardly directed Na^+ gradient (curve 6), suggesting that NCX_Mj functions as a Na^+/Ca^{2+} exchanger rather than a H^+/Ca^{2+} exchanger. To confirm the Na^+ selectivity for the exchange function of NCX_Mj, we performed another set of $^{45}Ca^{2+}$ flux assays using liposomes loaded with a buffer solution containing either Na^+, K^+, Li^+, or $NMDG^+$ as the only monovalent salt. The results clearly demonstrate that intraliposomal Na^+ facilitates the Ca^{2+} influx at a much higher rate than other monovalents (Fig. 1B). The commonly observed divalent cation blockage of NCX (i.e., by Cd^{2+}) (*26*) was also tested on NCX_Mj by performing the flux assay with $CdCl_2$ in the reaction buffer. Cd^{2+} exhibits a concentration-dependent blockage of Ca^{2+} influx with a half-inhibition concentration of ~0.4 mM under our experimental conditions (Fig. 1C). Consistent with the flux assay, the exchanger-mediated Ca^{2+} uptake or extrusion was also observed in NCX_Mj expressing *Escherichia coli* cells (see supporting online material text and fig. S1).

Structural determination of NCX_Mj. We used two crystallization approaches to obtain the structure of NCX_Mj (*25*). First, the crystals were grown in the lipidic cubic phase (LCP), following a similar protocol as previously described (*27*). The LCP crystallization yielded well-diffracting crystals large enough for complete data collection with a single crystal. The crystals are of the $P2_12_12_1$ space group, with one subunit per asymmetric unit. The structure was determined by single isomorphous replacement with anomalous scattering using samarium derivatized crystals and refined to 1.9 Å (table S1). Second, a conventional crystallization approach using sitting drop vapor diffusion yielded NCX_Mj crystals in detergent, and the structure was determined at 3.6 Å using molecular replacement. The crystal structures obtained from both methods are virtually identical, demonstrating that NCX_Mj maintains the same structure in both detergent and lipid environments. Though the discussion focuses primarily on the LCP crystal structure, the lower-resolution structures in detergent provide important insight into the divalent blockage site of NCX_Mj.

Overall structure of NCX_Mj. NCX_Mj exists as a monomer in both crystal forms and contains 10 transmembrane (TM) helices, with both termini on the extracellular side (Fig. 2A and figs. S2 and S3), consistent with the predicted topology for YrbG, an NCX homolog from *E. coli* (*28*). Based on the similarity in sequence and hydrophobicity pattern between NCK_Mj and its eukaryotic counterparts, the eukaryotic NCX is likely to share the same 10-TM topology rather than the previously predicted 9-TM topology (fig. S2). Eight of the 10 helices (TMs 2 to 5 and 7 to 10) form a tightly packed core perpendicularly embedded in the membrane. TMs 1 and 6, on the other hand, are exceptionally long, with ~35 residues in each helix. They are oriented at an angle of ~45° to the membrane surface and appear to be loosely packed against the core. The two highly conserved α repeats, consisting of TMs 2 and 3 for α1 and TMs 7 and 8 for α2, are bundled in the center of the protein and surrounded by the other helices (Fig. 2B and fig. S3B). All α-repeat helices are bent into two (for TMs 3 and 8) or three (for TMs 2 and 7) segments (labeled alphabetically in Fig. 2A and fig. S2), creating a pocket in the middle of the bundle where Na^+ and Ca^{2+} bind. Beyond sequence homology, the N-terminal half of the protein shares a similar structure to the C-terminal half but with opposite topology, as though the two halves are related by a molecular dyad (Fig. 2C and fig. S3). Although structural repeats of 5-TM helices have been observed in other membrane transporters (*29*, *30*), the NCX_Mj structure represents a new fold, as a search of the structure database using DALI (*31*) yields no similar structures. The linker between the two halves in NCX_Mj is a short and disordered loop from residues 149 to 155. The equivalent linker in eukaryotic NCX is expected to be the large intracellular regulatory domain.

Na^+ and Ca^{2+} binding sites. The high-resolution structure reveals four potential cation binding sites in the protein core, at the center of the membrane (Fig. 2A). The four sites are arranged in a diamond shape, with the sites nearest to the extracellular and intracellular face labeled S_{ext} and S_{int}, respectively, and the two middle sites designated as S_{mid} and S_{Ca}, as the latter is the Ca^{2+}-specific site (Fig. 3, A and B). All residues participating in ion binding are from the two α repeats and are highly conserved in both the NCX and NCKX families of proteins (fig. S2), and mutating these residues in eukaryotic NCX leads to the loss of ion-exchange functions (*22*).

Both S_{ext} and S_{int} are surrounded by five oxygen ligands and share identical ligand chemistry

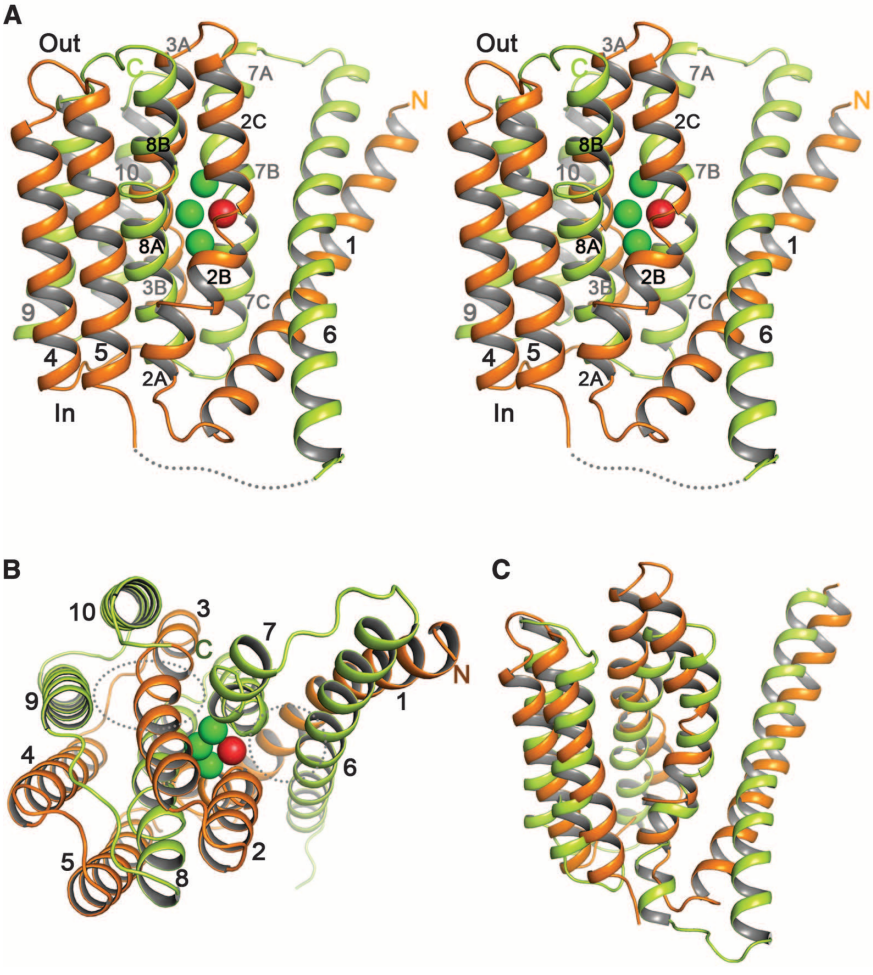

Fig. 2. Overall structure of NCX_Mj. (**A**) Stereo view of NCK_Mj viewed from the membrane. The N- and C-terminal halves are shown as orange and green ribbons, respectively. The four ion-binding sites are shown as green spheres for Na^+ and red spheres for Ca^{2+}. The dotted line represents the disordered loop between TMs 5 and 6. (**B**) View of NCX_Mj from the extracellular side. The dotted circle and oval indicate the entryways of external passages for Ca^{2+} and Na^+, respectively. (**C**) Superimposition between the N-terminal half (orange) of NCX_Mj and its inverted C-terminal half (green). All structure figures were generated in PyMOL (*40*).

as well as geometry, with ion-ligand distances all within the range of 2.3 to 2.5 Å (Fig. 3A and fig. S4). The coordination number, ligand chemistry, and ion-ligand distances of both sites are consistent with Na^+ binding (*32*). Although Ca^{2+} has the same size and ion-ligand distances as Na^+, it tends to have more than five ligands for optimal coordination (*33*, *34*). The S_{Ca} site is surrounded by six oxygen ligands within the distances of 2.3 to 2.6 Å: two from the backbone carbonyls of Thr^{50} and Thr^{209} and four from the carboxylates of Glu^{54} and Glu^{213}; all are contributed by the signature sequence of GTSLPE (*35*) within the two α repeats. The coordination number, ion-ligand distances, and bidentate ion chelation of the two acidic side-chain carboxylates at the S_{Ca} site are characteristic of Ca^{2+} binding (*33*, *34*). To confirm that the density at S_{Ca} is from Ca^{2+}, we also collected diffraction data at a wavelength of 2.0 Å to optimize Ca^{2+} anomalous scattering. Anomalous signal is observed at the S_{Ca} site in the anomalous-difference map (Fig. 3C), confirming the specificity of Ca^{2+} binding at this site. Surrounded by the side chains of Glu^{54}, Asn^{81}, Glu^{213}, and Asp^{240}, the S_{mid} site has only four oxygen ligands within a 3 Å distance and does not appear to be optimal for either Na^+ or Ca^{2+} binding. As tetradentate ion binding is common for Na^+ but rare for Ca^{2+}, we suggest that this suboptimal site allows Na^+ binding at high concentration, which, along with S_{ext} and S_{int}, accommodates three Na^+ ions during the ion-exchange reaction. As further evidence of non-specificity at S_{mid}, we identified it as the divalent blockage site from the structure of NCX_Mj obtained by the conventional crystallization approach. In these crystals, $CdCl_2$ or $MnCl_2$ were essential additives for crystallization, and their binding at S_{mid} was determined from the anomalous-difference Fourier map (Fig. 3D). Without directly competing for the S_{Ca} site, the divalent blockers occupy the neighboring, less selective S_{mid} site, which in turn weakens or abolishes Ca^{2+} binding at S_{Ca} and may also block Na^+ translocation.

Several features of this cluster of four ion-binding sites are noteworthy and clearly related to the Na^+/Ca^{2+}-exchange function of the NCX family. First, the four sites are related by a two-fold rotational axis connecting S_{mid} and S_{Ca}, which coincides with the pseudomolecular dyad of the protein. Second, several ligands are shared by multiple sites, most notably the side-chain carboxylates from Glu^{54} and Glu^{213}, which are shared by S_{mid}, S_{Ca}, and S_{ext} (for E54) or S_{int} (for E213) (Fig. 3A and fig. S4). Third, all four sites are in close proximity, with the shortest distance of ~3.6 Å between the two middle sites (S_{mid} and S_{Ca}) (Fig. 3B). Furthermore, the proximity and presence of only three negatively charged ligands indicate that all four sites are unlikely to be occupied simultaneously. Indeed, the Fo-Fc ion-omit map clearly shows different intensity of the electron density at each site, indicating different ion occupancy (Fig. 3A).

Ion-permeation pathways and inward-outward conformational change. The NCX_Mj structure likely represents an outward-facing conformation, as two deep cavities are observed on the extracellular surface of the protein, penetrating into the protein core where Na^+ and Ca^{2+} bind and providing two independent solvent-accessible passageways for external ion access (Figs. 2B and 4A and fig. S5). One passage, surrounded by the external halves of TMs 3 (3A segment), 7 (7A and 7B segments), 9, and 10, connects the extracellular solvent to the Na^+-specific S_{ext} site. The other passage is partially surrounded by the external halves of TMs 2 (2C segment), 6, and 7 (7A and 7B segments), with an open gap between TMs 2 and 6, which is probably sealed off by the extracellular leaflet of membrane lipids, as acyl chains from monoolein were observed in the structure. This passageway allows Ca^{2+} access from the extracellular solvent to the Ca^{2+}-specific S_{Ca} site.

Whereas the NCX_Mj structure adopts an outward-facing conformation, several structural and functional features allow us to generate a feasible structure model for the inward-facing conformation. The symmetry of NCX_Mj and its ion-binding sites, as well as the bidirectional ion exchange, would suggest that the inward-facing model should maintain similar symmetry and ion accessibility but with ion-permeation pathways directed toward the intracellular side, analogous to an inverted structure of NCX_Mj. In addition, rapid bidirectional ion exchange requires a rapid conformational change between the inward- and outward-facing states, implying equivalent stability with a low-energy barrier to the transition, thus precluding a dramatic structural change between the two conformations. A superimposition of NCX_Mj and its inverted structure shows a near-perfect structural alignment over the α-repeat helix bundle but different positions for the peripheral helices of TMs 1 and 2A, as well as TMs 6 and 7A (fig. S6). The inward-facing model was generated by simply swapping these two helical regions as depicted (fig. S6). Similar approaches have been used to generate putative models in other secondary solute transporters with inverted structural repeats (*36*, *37*).

Compared to the outward-facing NCX_Mj, the inward-facing model maintains the same tightly

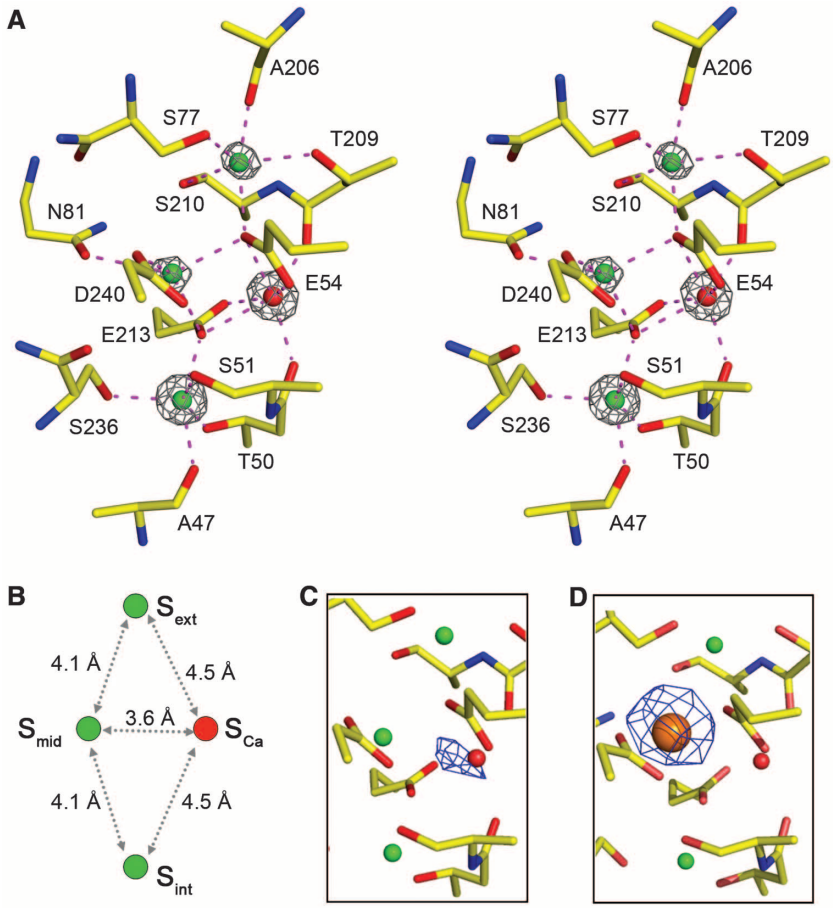

Fig. 3. Ion-binding sites of NCX_Mj. (**A**) Stereo view of the ion-binding sites. Green and red spheres represent Na^+ and Ca^{2+}, respectively. Gray mesh depicts electron density calculated from the F_o-F_c ion-omit map and contoured at 9σ. (**B**) Distances between adjacent ion-binding sites. (**C**) Density (blue mesh, contoured at 3.5σ) from the anomalous-difference Fourier map calculated using diffraction data of a LCP crystal at 2 Å wavelength indicates Ca^{2+} binding at the S_{Ca} site. (**D**) Density (blue mesh, contoured at 8σ) of bound Cd^{2+} (orange sphere) at the S_{mid} site from the anomalous-difference Fourier map. Diffraction data were collected at 2.0 Å from crystals grown in the presence of 10 mM $CdCl_2$ using the conventional crystallization method. Data from Mn^{2+}-containing crystals gave the same result.

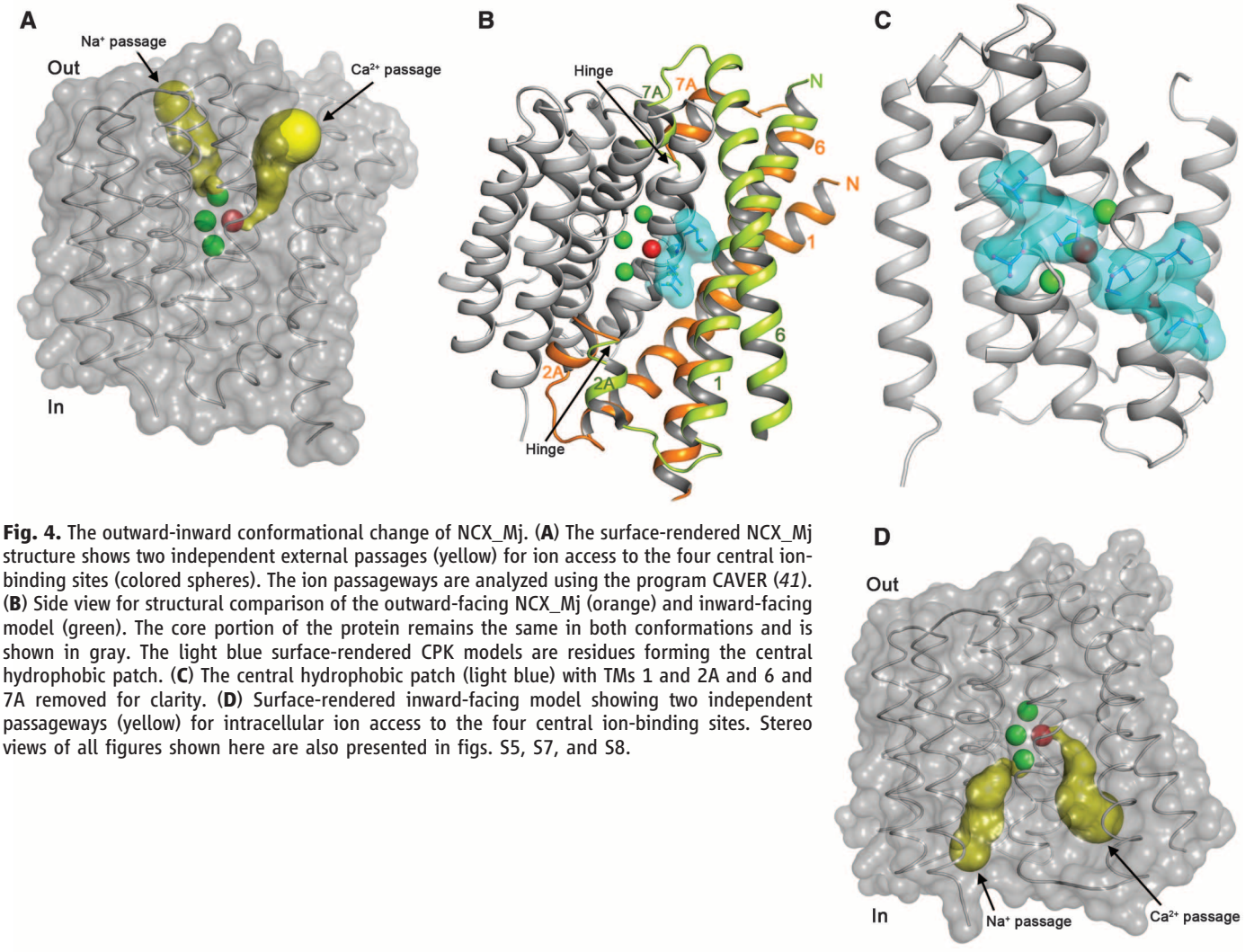

Fig. 4. The outward-inward conformational change of NCX_Mj. (**A**) The surface-rendered NCX_Mj structure shows two independent external passages (yellow) for ion access to the four central ion-binding sites (colored spheres). The ion passageways are analyzed using the program CAVER (*41*). (**B**) Side view for structural comparison of the outward-facing NCX_Mj (orange) and inward-facing model (green). The core portion of the protein remains the same in both conformations and is shown in gray. The light blue surface-rendered CPK models are residues forming the central hydrophobic patch. (**C**) The central hydrophobic patch (light blue) with TMs 1 and 2A and 6 and 7A removed for clarity. (**D**) Surface-rendered inward-facing model showing two independent passageways (yellow) for intracellular ion access to the four central ion-binding sites. Stereo views of all figures shown here are also presented in figs. S5, S7, and S8.

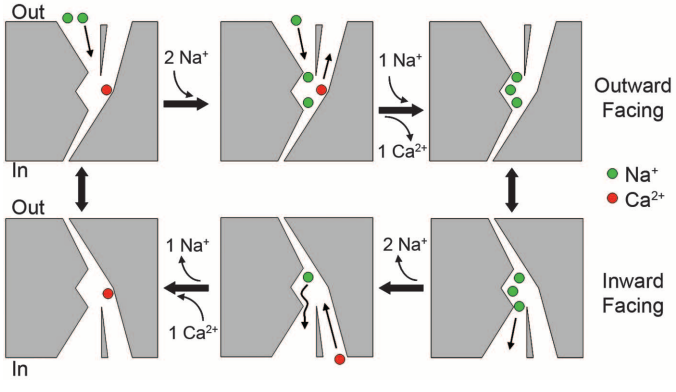

Fig. 5. Cartoon representation of Na^+/Ca^{2+} exchange of NCX in the classical $3Na^+$:$1Ca^{2+}$ extrusion mode.

packed core and ion-binding sites but has different packing between the peripheral helices (TMs 1, 2A, 6, and 7A) and the core (Fig. 4B and fig. S7). Without obvious steric clash, the inward-facing model retains similar hydrophobic-packing interactions between these helices and the core. The movement of TMs 1, 2A, 6, and 7A is hinged at the bends between TMs 2A and 2B and TMs 7A and 7B, and it may involve sliding across a central flat hydrophobic patch that is centered about the conserved Pro residues from the signature sequence motifs of the α repeats (Fig. 4C and fig. S8). Consequently, this proposed conformational change leads to the closure of the two outward-facing ion passageways and the formation of two inward-facing ones connecting the S_{int} and S_{Ca} sites, respectively, to the intracellular side (Fig. 4D and fig. S5B). With a simple sliding motion primarily involving two loosely packed helices, the outward and inward conformations can rapidly interchange, coupling to the alternative access of the four ion-binding sites from each side, consistent with the mechanism of rapid consecutive ion-exchange reaction in NCX (*3*, *8*, *38*, *39*).

Na^+/Ca^{2+}-exchange mechanisms. The arrangement of four central ion-binding sites with differing specificity and their alternating accessibility from each side upon conformational change reveal the structural mechanism of Na^+/Ca^{2+} exchange in NCX. Among the four sites, only S_{Ca} is specific for Ca^{2+} binding, whereas the other three are designed for Na^+ binding under physiological conditions, and their occupancy depends on the Na^+ concentration. Whereas S_{Ca} is alternatively accessible from each side, the three Na^+ sites are aligned in a winding single file with only one end being accessible in a given conformation: S_{ext} when facing outward and S_{int} when facing inward. Positioning these two identical, Na^+-specific sites on both ends ensures the selective and bidirectional Na^+/Ca^{2+}-exchange function in NCX.

The cluster of four sites in close proximity and ligand-sharing features in NCX_Mj lead us to propose a progressive antagonist effect of multiple Na^+ binding on Ca^{2+} affinity as depicted in the

cartoon representation of a simplified Na^+/Ca^{2+}-exchange reaction in the classic Ca^{2+} extrusion mode (Fig. 5). Starting with the Ca^{2+} bound, outward-facing conformation, the exchange reaction is initiated by the entry of Na^+ from the extracellular side, probably occupying the Na^+-optimized S_{int} and S_{ext} sites first. As each site competes for a negatively charged ligand with S_{Ca}, the binding of these two Na^+ ions decreases the Ca^{2+} affinity at S_{Ca} but may be insufficient for Ca^{2+} release due to the presence of high extracellular Ca^{2+} under physiological conditions. With a high external Na^+ concentration ($[Na^+]_0$), the entry of a third Na^+ ion increases Na^+ occupancy at S_{mid}, which further reduces the Ca^{2+} affinity and results in Ca^{2+} release to the extracellular side. Upon conformational change to an inward-facing state, the three bound Na^+ ions are exposed to the low intracellular $[Na^+]_i$ environment. As a weak binding site, the S_{mid} Na^+ is likely released first, possibly along with the S_{int} Na^+. The release of the bound Na^+ restores the high-affinity Ca^{2+} binding at S_{Ca}, which in turn leads to the release of the third Na^+ from S_{ext}. The conformational change reverting NCX_Mj to the Ca^{2+}-bound outward-facing state completes the cycle. This sequential binding of three Na^+ ions for the release of one Ca^{2+} explains the 3:1 stoichiometry of the Na^+/Ca^{2+}-exchange reaction and the cooperativity of Na^+ binding in activating Ca^{2+} release. This simplified exchange mechanism does not preclude other exchange ratios (*13*). For example, at high extracellular $[Na^+]_o$, the vacant S_{Ca} site upon Ca^{2+} release could also be occupied by a Na^+, resulting in a translocation of four Na^+ ions to the intracellular side. Likewise, depending on the Na^+ and Ca^{2+} concentrations, the bound Na^+ may not be completely unloaded upon Ca^{2+} binding from the intracellular side. The coexistence of these possibilities in the same transporter leads to a more complex process of Na^+/Ca^{2+} exchange and may explain the variability of the exchange ratios observed under different experimental conditions.

References and Notes

1. D. E. Clapham, *Cell* **131**, 1047 (2007).
2. M. J. Berridge, M. D. Bootman, H. L. Roderick, *Nat. Rev. Mol. Cell Biol.* **4**, 517 (2003).
3. M. P. Blaustein, W. J. Lederer, *Physiol. Rev.* **79**, 763 (1999).
4. K. D. Philipson, D. A. Nicoll, *Annu. Rev. Physiol.* **62**, 111 (2000).
5. R. DiPolo, L. Beaugé, *Physiol. Rev.* **86**, 155 (2006).
6. D. A. Nicoll, S. Longoni, K. D. Philipson, *Science* **250**, 562 (1990).
7. D. W. Hilgemann, *Biophys. J.* **71**, 759 (1996).
8. D. W. Hilgemann, D. A. Nicoll, K. D. Philipson, *Nature* **352**, 715 (1991).
9. J. P. Reeves, C. C. Hale, *J. Biol. Chem.* **259**, 7733 (1984).
10. M. P. Blaustein, J. M. Russell, *J. Membr. Biol.* **22**, 285 (1975).
11. H. Rasgado-Flores, M. P. Blaustein, *Am. J. Physiol.* **252**, C499 (1987).
12. J. Kimura, A. Noma, H. Irisawa, *Nature* **319**, 596 (1986).
13. T. M. Kang, D. W. Hilgemann, *Nature* **427**, 544 (2004).
14. D. Noble, *Science* **295**, 1678 (2002).
15. Y. Watanabe, Y. Koide, J. Kimura, *J. Pharmacol. Sci.* **102**, 7 (2006).
16. D. A. Nicoll, M. Ottolia, K. D. Philipson, *Ann. N. Y. Acad. Sci.* **976**, 11 (2002).
17. X. Ren, D. A. Nicoll, L. Xu, Z. Qu, K. D. Philipson, *Biochemistry* **49**, 8585 (2010).
18. D. W. Hilgemann, *Nature* **344**, 242 (1990).
19. S. Matsuoka, D. A. Nicoll, R. F. Reilly, D. W. Hilgemann, K. D. Philipson, *Proc. Natl. Acad. Sci. U.S.A.* **90**, 3870 (1993).
20. E. M. Schwarz, S. Benzer, *Proc. Natl. Acad. Sci. U.S.A.* **94**, 10249 (1997).
21. X. Cai, J. Lytton, *Mol. Biol. Evol.* **21**, 1692 (2004).
22. D. A. Nicoll, L. V. Hryshko, S. Matsuoka, J. S. Frank, K. D. Philipson, *J. Biol. Chem.* **271**, 13385 (1996).
23. H. F. Altimimi, P. P. Schnetkamp, *Channels (Austin)* **1**, 62 (2007).
24. H. Reiländer *et al.*, *EMBO J.* **11**, 1689 (1992).
25. Materials and methods are available as supporting material on *Science* Online.
26. T. L. Trosper, K. D. Philipson, *Biochim. Biophys. Acta* **731**, 63 (1983).
27. M. Caffrey, V. Cherezov, *Nat. Protoc.* **4**, 706 (2009).
28. A. Sääf, L. Baars, G. von Heijne, *J. Biol. Chem.* **276**, 18905 (2001).
29. S. Faham *et al.*, *Science* **321**, 810 (2008).
30. A. Yamashita, S. K. Singh, T. Kawate, Y. Jin, E. Gouaux, *Nature* **437**, 215 (2005).
31. L. Holm, P. Rosenström, *Nucleic Acids Res.* **38**, W545 (2010).
32. M. M. Harding, *Acta Crystallogr. D Biol. Crystallogr.* **58**, 872 (2002).
33. A. K. Katz, J. P. Glusker, S. A. Beebe, C. W. Bock, *J. Am. Chem. Soc.* **118**, 5752 (1996).
34. E. Pidcock, G. R. Moore, *J. Biol. Inorg. Chem.* **6**, 479 (2001).
35. Single-letter abbreviations for the amino acid residues are as follows: A, Ala; C, Cys; D, Asp; E, Glu; F, Phe; G, Gly; H, His; I, Ile; K, Lys; L, Leu; M, Met; N, Asn; P, Pro; Q, Gln; R, Arg; S, Ser; T, Thr; V, Val; W, Trp; and Y, Tyr.
36. L. R. Forrest *et al.*, *Proc. Natl. Acad. Sci. U.S.A.* **105**, 10338 (2008).
37. N. J. Hu, S. Iwata, A. D. Cameron, D. Drew, *Nature* **478**, 408 (2011).
38. D. Khananshvili, *Biochemistry* **29**, 2437 (1990).
39. M. A. Milanick, M. D. S. Frame, *Ann. N. Y. Acad. Sci.* **639**, 604 (1991).
40. W. L. DeLano, PyMOL (DeLano Scientific, San Carlos, CA, 2002); www.pymol.org.
41. M. Petřek *et al.*, *BMC Bioinformatics* **7**, 316 (2006).

Acknowledgments: We thank D. Rosenbaum for technical support with LCP crystallization, D. Hilgemann for discussion, and N. Nguyen for critical review of the manuscript. Structures shown in this report are derived from work performed at the Advanced Photon Source (19-ID and 23-ID beamlines), Argonne National Laboratory. Use of the Advanced Photon Source, an Office of Science User Facility operated for the U.S. Department of Energy (DOE) Office of Science by Argonne National Laboratory, was supported by the U.S. DOE under contract no. DE-AC02-06CH11357. We thank the beamline staff for assistance in data collection. This work was supported in part by the Howard Hughes Medical Institute and by grants from the David and Lucile Packard Foundation and the Welch Foundation (grant I-1578 to Y.J.). The atomic coordinates and structural factors have been deposited in the Protein Data Bank with the accession numbers 3V5U for the LCP crystal and 3V5S for the low-resolution crystal in detergent. The authors declare no competing financial interests.

Supporting Online Material

www.sciencemag.org/cgi/content/full/335/6069/686/DC1
Materials and Methods
SOM Text
Figs. S1 to S9
Table S1
References (*42*–*56*)

25 October 2011; accepted 21 December 2011
10.1126/science.1215759

REPORTS

One-Step Fabrication of Supramolecular Microcapsules from Microfluidic Droplets

Jing Zhang,[1] Roger J. Coulston,[1,2] Samuel T. Jones,[1,2] Jin Geng,[1,2] Oren A. Scherman,[1,2]* Chris Abell[1]*

Although many techniques exist for preparing microcapsules, it is still challenging to fabricate them in an efficient and scalable process without compromising functionality and encapsulation efficiency. We demonstrated a simple one-step approach that exploits a versatile host-guest system and uses microfluidic droplets to generate porous microcapsules with easily customizable functionality. The capsules comprise a polymer-gold nanoparticle composite held together by cucurbit[8]uril ternary complexes. The dynamic yet highly stable micrometer-sized structures can be loaded in one step during capsule formation and are amenable to on-demand encapsulant release. The internal chemical environment can be probed with surface enhanced Raman spectroscopy.

The encapsulation of materials for protection and phase separation has evolved into a major interdisciplinary research focus (*1*, *2*). Synthetic microcapsules (*3*, *4*), in which the composition of the shell structure and the core content can be controlled, have found importance in applications as diverse as cell encapsulation (*5*, *6*), drug delivery (*7*), diagnostics (*8*), catalysis (*9*), food additives (*10*), and electronic displays (*11*). Preparation of conventional polymeric microcapsules via the layer-by-layer (L-b-L) technique (*12*, *13*), although powerful, suffers from reduced encapsulation efficiencies as a result of postfabrication loading. Alternative self-assembly processes, either by forming polymersomes (*14*) or by colloidal emulsion-templating (*15*, *16*), still lack monodispersity, stability, high loading efficiency, and material diversity in the resulting microcapsules, restricting their function

[1]Department of Chemistry, University of Cambridge, Lensfield Road, Cambridge CB2 1EW, UK. [2]Melville Laboratory for Polymer Synthesis, Department of Chemistry, University of Cambridge, Lensfield Road, Cambridge CB2 1EW, UK.

*To whom correspondence should be addressed. E-mail: oas23@cam.ac.uk (O.A.S.); ca26@cam.ac.uk (C.A.)